Impact of Tellurium Precipitates in CdZnTe Substrates on MBE HgCdTe Deposition

J.D. BENSON,[1,5,6] L.O. BUBULAC,[1] P.J. SMITH,[1] R.N. JACOBS,[1]
J.K. MARKUNAS,[1] M. JAIME-VASQUEZ,[1] L.A. ALMEIDA,[1] A. STOLTZ,[1]
P.S. WIJEWARNASURIYA,[2] G. BRILL,[2] Y. CHEN,[2] J. PETERSON,[3]
M. REDDY,[3] M.F. VILELA,[3] S.M. JOHNSON,[3] D.D. LOFGREEN,[3]
A. YULIUS,[4] G. BOSTRUP,[4] M. CARMODY,[4] D. LEE,[4] and S. COUTURE[4]

1.—U. S. Army RDECOM, CERDEC Night Vision and Electronic Sensors Directorate, Ft. Belvoir, VA, USA. 2.—U. S. Army Research Laboratory, Adelphi, MD, USA. 3.—Raytheon Vision Systems, Goleta, CA, USA. 4.—Teledyne Imaging Sensors, Camarillo, CA, USA. 5.—e-mail: david.j.benson@us.army.mil. 6.—e-mail: j.d.benson6.civ@mail.mil

State-of-the-art (112)B CdZnTe substrates were examined for near-surface tellurium precipitate-related defects. The Te precipitate density was observed to be fairly uniform throughout the bulk of the wafer, including the near-surface region. After a molecular beam epitaxy (MBE) preparation etch, exposed Te precipitates, small pits, and bumps on the (112)B surface of the CdZnTe wafer were observed. From near-infrared and dark field microscopy, the bumps and small pits on the CdZnTe surface are associated with strings of Te precipitates. Raised bumps are Te precipitates near the surface of the (112)B CdZnTe where the MBE preparation etch has not yet exposed the Te precipitate(s). An exposed Te precipitate sticking above the etched CdZnTe surface plane occurs when the MBE preparation etch rapidly undercuts a Te precipitate. Shallow surface pits are formed when the Te precipitate is completely undercut from the surrounding (112)B surface plane. The Te precipitate that was previously located at the center of the pit is liberated by the MBE preparation etch process.

Key words: HgCdTe/CdZnTe, molecular beam epitaxy, Te precipitate, macro- and micro-defects

INTRODUCTION

The highest sensitivity, lowest dark current HgCdTe infrared focal plane arrays (IRFPAs) are currently produced on CdZnTe substrates. The performance and operability for next generation IRFPAs on CdZnTe substrates is believed to be impacted by Te precipitate variability. Te precipitates impact molecular beam epitaxy (MBE) HgCdTe/CdZnTe IRFPA performance by two opposing methods: (1) getter impurities from substrate and epilayer during deposition and processing, and (2) they are the presumed origin of some of the MBE deposition defects.

It is well known that CdZnTe substrates have Te precipitates.[1–4] Te precipitates are known to getter impurities in the CdZnTe substrates and prevent impurities from reaching the deposited HgCdTe epitaxial thin films.[5–10] Impurities in CdZnTe substrates can diffuse into HgCdTe deposited on these substrates by liquid phase epitaxy, metal–organic chemical vapor deposition, or MBE.[1] Impurities diffusing from the CdZnTe substrate can affect carrier concentration, mobility, and minority carrier lifetime in the HgCdTe epilayer.[6] The density and size of Te precipitates in CdZnTe has further been demonstrated to impact the electrical transport properties of deposited HgCdTe.[5] The typical Te precipitate density in state-of-the-art CdZnTe is $\sim 2 \times 10^6$ cm^{-3}. The typical Te precipitate diameter in state-of-the-art CdZnTe is $\sim$2–3 μm.
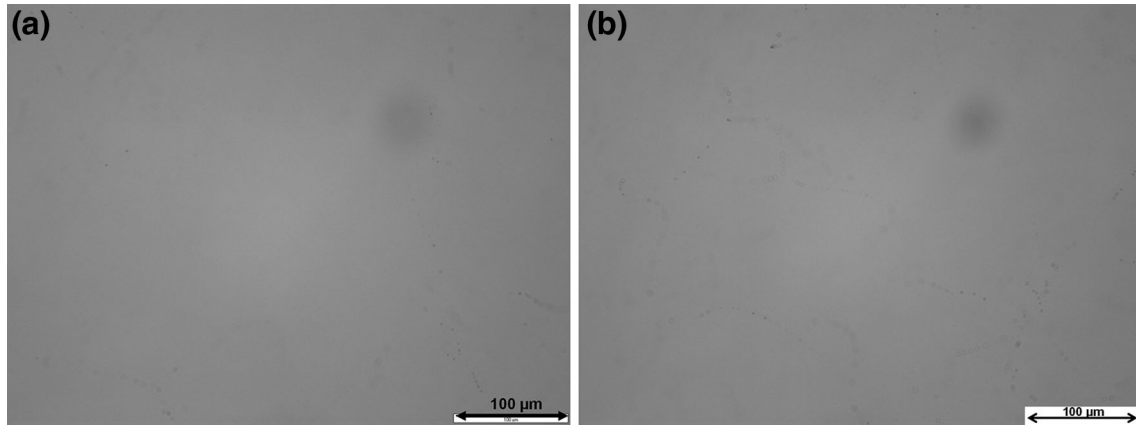
Fig. 1. Near-IR microscopy images of Te precipitate density and distribution near the center of a 2 × 3 cm (112)B CdZnTe substrate. Image area is 512.2 × 382.7 μm. (a) The (112)B surface; (b) $\sim$230 μm below the (112)B surface.

It has also been demonstrated that Te precipitate-related defects near the growth surface of the (112)B CdZnTe substrate affect MBE-deposited HgCdTe epilayers.[11–14] The goal of this effort is to analyze the formation of Te precipitate-related defects in (112)B CdZnTe substrates.

EXPERIMENTAL SETUP

Nominal (112) CdZnTe substrates from Nikko Materials[15] were analyzed in this work. Nomarski phase contrast microscopy was used to locate morphological defects on the substrate surface. Atomic force microscopy (AFM) and scanning profilometry were used to characterize the surface topography of the Te precipitates and morphological defects in the CdZnTe substrates. Near-infrared (near-IR) transmission and dark field microscopy were utilized to observe Te precipitate size and density as well as to correlate with surface defects.

RESULTS

A yield-limiting factor in MBE HgCdTe/CdZnTe detector fabrication is the presence of macro-defects.[11] Macro-defects have been classified into 4 categories: large defects, voids, micro-voids, and morphological defects.[13] Large defects and voids range in size from $\sim$1 to several hundred μm. Large defects and voids have been linked to non-optimized MBE growth conditions and volatile particulate contamination.[11,13,16–18] Thus, their formation will not be addressed by this effort. Micro-voids are typically less than 10 μm in length and have a distinctive triangular shape. Minimum micro-void defect density is $\sim$1 × 10^3 cm^{-2} (typical micro-void defect density range is 1 × 10^3–1 × 10^5 cm^{-2} dependent on MBE growth conditions).[13] Cross-sectional transmission electron microscopy (TEM) analysis traced micro-void defects to pits on the surface of the (112)B CdZnTe substrate.[12] Morphological defects in MBE HgCdTe/CdZnTe are typically raised

structures from $\sim$1 to 50 μm. TEM analysis traced morphological defects to raised protrusions on the surface of the (112)B CdZnTe substrate.[13] The variation of morphological defect size in the MBE HgCdTe epilayer has been suggested to relate to the corresponding CdZnTe substrate bump size.[13] Morphological defects have no significant increase in EPD or the increase is confined to the proximity of bump/micro-void area. The objective of this research is to analyze Te precipitate-related defects, particularly small pits and raised protrusions, in (112)B CdZnTe substrates. It is anticipated that, by understanding the mechanisms responsible for these features in CdZnTe substrates, techniques can be found to minimize their formation. The minimization of small pits and raised protrusions in CdZnTe substrates should lead to a reduction in micro-voids and morphological defects in MBE HgCdTe/CdZnTe, which should in turn increase FPA operability.

Figure 1 shows near-IR microscopy images of the state-of-the-art Te precipitate density and distribution in (112) CdZnTe substrates. These images are from the center of a 2 × 3 cm 775-μm-thick (112) CdZnTe substrate. These two images are from a series of 52 near-IR microscopy images focusing through the complete depth of the CdZnTe substrate. Each image in the series was $\sim$15 μm deeper into the wafer. As observed in Fig. 1a and b, 'strings' of Te precipitates are observed. These 'strings' of Te precipitates are believed to follow low angle grain boundaries in CdZnTe.[14] Examining all 52 near-IR images reveals that the Te precipitate density is fairly uniform throughout the bulk of the wafer. Near-IR microscopy images also demonstrate that Te precipitate density in the near-surface region (top $\sim$5 μm of the (112)B surface) are laterally fairly uniform and equivalent to the density in the bulk of the substrate. There was an average of 15 Te precipitates in focus per near-IR image for the CdZnTe substrates measured. This uniformity of Te
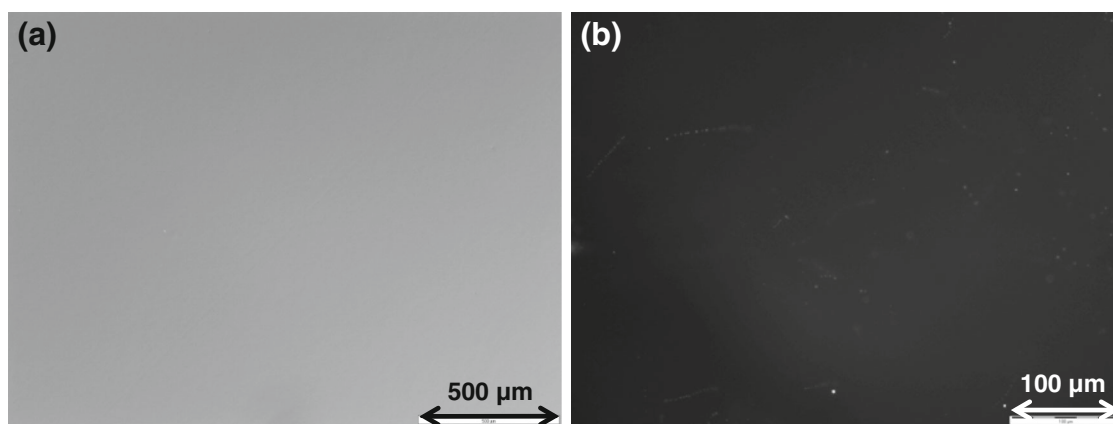
Fig. 2. Nomarski phase contrast (a) and dark field (b) microscopy images near the center of a 2 × 3 cm (112) CdZnTe substrate.
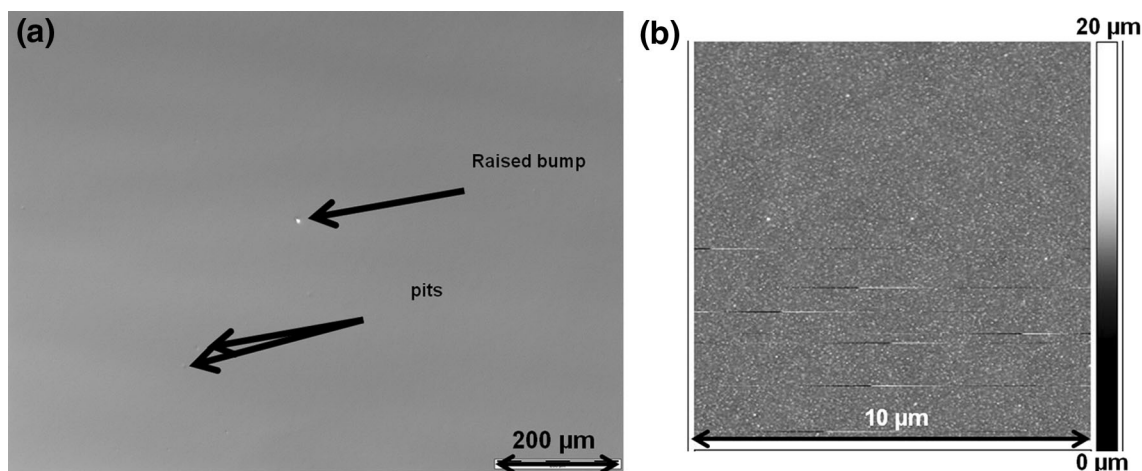

Fig. 3. Nomarski phase contrast (a) and AFM (b) images from the (112)B surface of a MBE preparation etched (112)B CdZnTe substrate.

precipitate density demonstrates that the average aerial density of precipitates at the surface of the wafer is the volume density × diameter of a Te precipitate. There are, however, instances in a single near-IR image (both in the near-surface region and in the bulk) of several 'strings' of Te precipitates intersecting at a shallow angle as shown in Fig. 1b.

Figure 2 shows typical images from the surface of an as-received wafer. The highly polished (112)B wafer surface is very smooth. Average surface roughness as determined by AFM is ~0.3 nm. Because of the smooth highly polished surface, Nomarski phase contrast microscopy detects very few defects, as shown in Fig. 2a. Dark field microscopy (of the same area at enhanced resolution) in Fig. 2b is able to detect a few more surface defects, but the surface generally still displays a very low morphological defect density. Dark field microscopy additionally displays Te precipitates and Te precipitate 'strings' in the near (112)B-surface region.

A MBE preparation/clean-up etch is required before epitaxial deposition of HgCdTe on a CdZnTe substrate. The MBE preparation/clean-up etch technique used in this work follows standard procedures: solvent soak, Br: methanol etch, solvent soak, N_2 blow dry, and mounting to a wafer holder.[19] The MBE preparation etch removes ~2–10 μm of CdZnTe from the surface.[19,20] The amount of CdZnTe removed is a function of the percentage of Br used and the etch time. The MBE preparation etch technique is used to reduce the native oxide on the CdZnTe wafer and remove any residual organic contamination.[19–22] The MBE preparation etch is also required to remove surface and near-surface damage induced to the CdZnTe crystal during wafer production.[23,24]

Figure 3 shows typical low surface defect density images from the (112)B CdZnTe surface of an MBE preparation etched wafer. As observed in Fig. 3a, a low density of small pits and bumps are seen on the (112)B surface after MBE preparation etch. After the MBE preparation etch technique, an average density of pits/bumps $\sim 3 \times 10^3$ cm^{-2} is observed. Figure 3b is an AFM image showing the smoothness

Benson, Bubulac, Smith, Jacobs, Markunas, Jaime-Vasquez, Almeida, Stoltz, Wijewarnasuriya, Brill, Chen, Peterson, Reddy, Vilela, Johnson, Lofgreen, Yulius, Bostrup, Carmody, Lee, and Couture
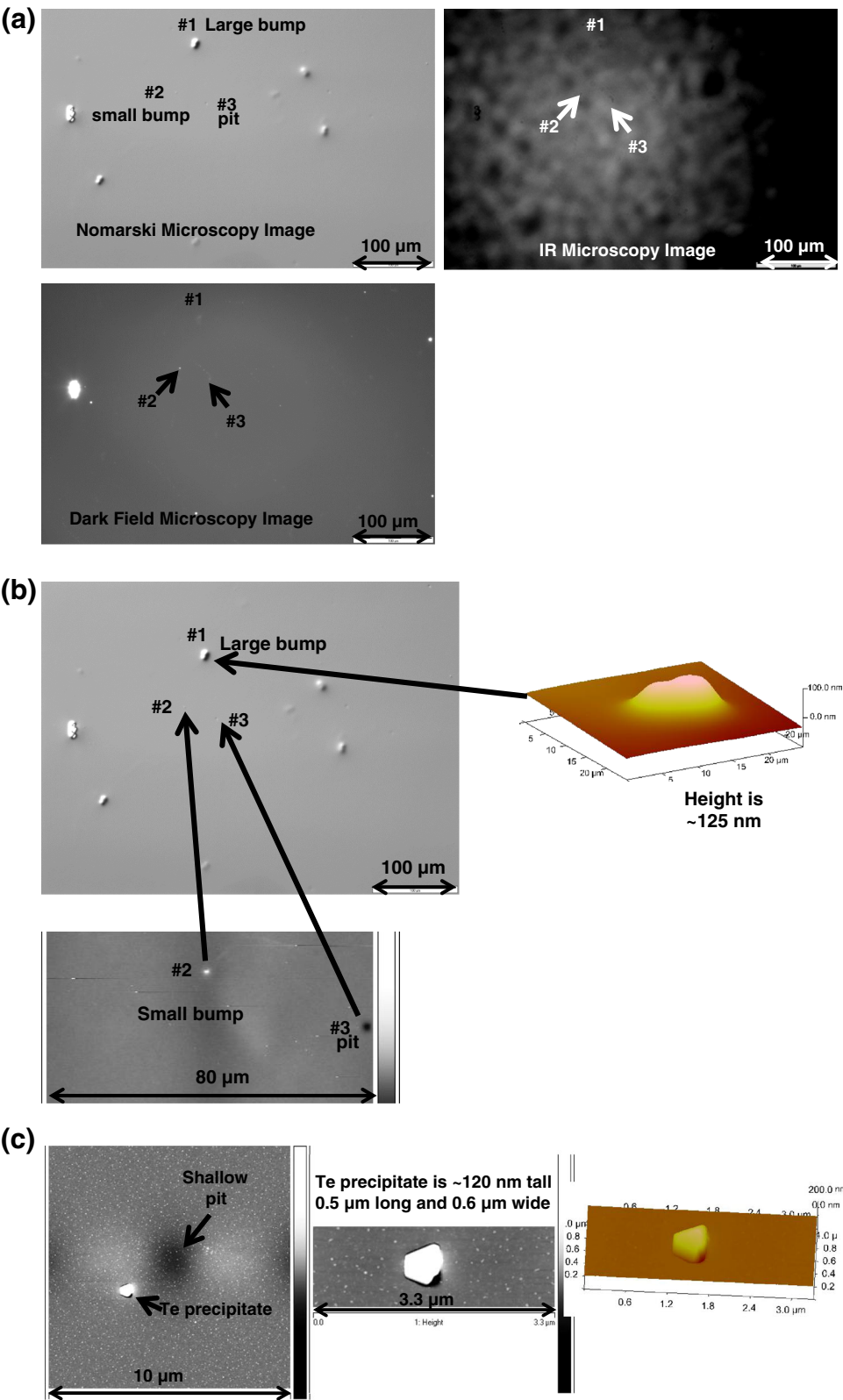

Fig. 4. Distinctive large bump cluster near the center of a 2 × 3 cm CdZnTe wafer after MBE preparation etch. (a) Nomarski phase contrast, near-IR, and dark field microscopy images of the distinctive bump cluster. (b) Nomarski phase contrast and AFM images of some of the bumps and pits. (c) High resolution AFM images of the pit and a Te precipitate exposed during the MBE preparation etching.

of post-MBE preparation etch (112)B CdZnTe surface. The RMS roughness of the surface is ~0.4 nm. To further investigate the observed pits and bumps on the MBE preparation etched CdZnTe wafer, a distinctive large bump cluster shown in Fig. 4 near the center of a 2 × 3 cm CdZnTe wafer was analyzed. The distinctive pattern of this large bump cluster enabled the correlation of Normarski phase contrast microscopy, dark field microscopy, near-IR microscopy, and AFM imaging of the same features. The images in Fig. 4 are from the same wafer that produced the images in Fig. 3—the large distinctive cluster was not typical of the MBE preparation etched wafer. From Fig. 4a, the near-IR and dark field microscopy images of the large (#1) and small (#2) bumps, and small pits (#3) demonstrate that they are all associated with 'strings' of Te precipitates that intersect with the surface. The large (#1) bump appears to be associated with the shallowest Te precipitate 'string'. In Fig. 4b, AFM measurements demonstrate that the large (#1) bump is ~120 nm tall and is composed of 2 adjoining hillocks with a total length of ~15 μm. The smaller (#2) bump was measured to be ~50 nm tall. The small pit (#3) was observed to be ~10 nm deep and ~1 μm in diameter. In Fig. 4c, high resolution AFM images of the small pit (#3) and the surrounding area show an exposed Te precipitate. The Te precipitate is believed to have been exposed by the MBE preparation etch. From the high resolution AFM images in Fig. 4c, the edges of the CdZnTe surrounding the Te precipitate have been preferentially etched.

From the above observations, the following hypotheses of the formation of raised bumps, shallow pits, and exposed Te precipitates on the surface of (112)B MBE preparation etched CdZnTe surfaces can be formulated. Firstly, the raised bumps are Te precipitates near the (112)B CdZnTe surface where the Br:methanol etch has not yet exposed the Te precipitate(s). The covered Te precipitate does not etch as rapidly as the surrounding material. Potential reasons for the etch rate difference could be the strain field caused by the Te precipitate or the overlaying CdZnTe is slightly mis-oriented or polycrystalline. Further experimentation is required to clarify this issue. Larger raised bumps are a result of a shallow Te precipitate string where multiple Te precipitates are in the near-surface region. Secondly, once the Te precipitate has been exposed by the Br:methanol MBE preparation etch, the Te precipitate is rapidly undercut. This leaves the exposed surface of the Te precipitate sticking above the MBE preparation etched surface plane. And thirdly, shallow surface pits are formed when Te precipitates are undercut from the surrounding MBE preparation etched (112)B surface plane. The Te precipitate located at the center of the pit is liberated during the MBE preparation etch process. This Te precipitate is dispersed in the MBE preparation etch liquid.

CONCLUSIONS

MBE HgCdTe/CdZnTe detector fabrication is currently limited by the presence of macro-defects. Te precipitate-related defects, particularly small pits and raised protrusions, in (112)B CdZnTe substrates have been previously linked to micro-void and morphological defects in the HgCdTe epilayer. In this work, the formation of Te precipitate-related defects, particularly small pits and raised protrusions, in (112)B CdZnTe substrates has been analyzed. Tellurium precipitate density was observed to be fairly uniform throughout the bulk of the wafer. From near-IR and dark field microscopy, the bumps and small pits are associated with strings of Te precipitates in the near-surface region. Pits and bumps were found after MBE preparation etching of the CdZnTe wafers. Raised bumps on the surface of the CdZnTe are defects where the MBE preparation etch does not remove material surrounding a Te precipitate as rapidly as the planar surface. Larger raised bumps are a result of a near-surface Te precipitate string. Exposed Te precipitates were observed to have been preferentially etched. Exposed Te precipitates have preferentially etched edges of the surrounding CdZnTe. Shallow pits are formed from undercut Te precipitates. The Te precipitate that was previously located at the center of the shallow pit is removed during the MBE preparation etch process.

The authors plan future experiments for the reduction/elimination of the Te precipitate-related defects described here. Potential ideas include: varying the percentage of Br, varying the etch time, use of different solvents (iso-propanol, ethylene glycol, etc) with Br, and alternate chemical etchants that do not contain Br. These different CdZnTe MBE preparation etches could minimize the small pits and raised protrusions in CdZnTe substrates. This should in turn lead to a reduction in micro-voids and morphological defects in MBE HgCdTe/CdZnTe, which should increase FPA operability.

REFERENCES

1. T.J. de Lyon, J.E. Jensen, M.D. Gorwitz, C.A. Cockrum, S.M. Johnson, and G.M. Venzor, *J. Electron. Mater.* 28, 705 (1999).
2. Y.P. Chen, G. Brill, E.M. Campo, T. Hierl, J.C.M. Hwang, and N.K. Dhar, *J. Electron. Mater.* 33, 498 (2004).
3. M. Carmody, J.G. Pasko, D. Edwall, M. Darasellia, L.A. Almeida, J. Molstad, J.H. Dinan, J.K. Markunas, Y. Chen, G. Brill, and N.K. Dhar, *J. Electron. Mater.* 33, 531 (2004).
4. M. Carmody, A. Yulius, D. Edwall, D. Lee, E. Piquette, R. Jacobs, J.D. Benson, A. Stoltz, J. Markunas, A. Almeida, and J. Arias, *J. Electron. Mater.* 41, 2719 (2012).
5. J.D. Benson, L.O. Bubulac, P.J. Smith, R.N. Jacobs, J.K. Markunas, M. Jaime-Vasquez, L.A. Almeida, A. Stoltz, J.M. Arias, G. Brill, Y. Chen, P.S. Wijewarnasuriya, S. Farrell, and U. Lee, *J. Electron. Mater.* 41, 2971 (2012).
6. L.O. Bubulac, J.D. Benson, R.N. Jacobs, A.J. Stoltz, M. Jaime-Vasquez, L.A. Almeida, A. Wang, L. Wang, R. Hellmer, T. Golding, J.H. Dinan, M. Carmody, P.S. Wijewarnasuriya, M.F. Lee, M.F. Vilela, J. Peterson, S.M. Johnson, D.F. Lofgreen, and D. Rhiger, *J. Electron. Mater.* 40, 280 (2011).
7. Y. Chen, S. Farrell, G. Brill, P. Wijewarnasuriya, and N. Dhar, *J. Cryst. Growth* 310, 5303 (2008).

8. M. Jaime-Vasquez, R.N. Jacobs, C. Nozaki, J.D. Benson, L.A. Almeida, J. Arias, and J. Pellegrino, *J. Electron. Mater.* 41, 2975 (2012).
9. H.R. Vydyanath, J.A. Ellsworth, J.B. Parkinson, J.J. Kennedy, B. Dean, C.J. Johnson, G.T. Neugebaur, J. Sepich, and P.K. Liao, *J. Electron. Mater.* 22, 1073 (1993).
10. T.S. Lee, J.W. Park, Y.T. Jeoung, H.K. Kim, C.H. Chun, J.M. Kim, I.H. Park, J.M. Chang, S.U. Kim, and M.J. Park, *J. Electron. Mater.* 24, 1053 (1995).
11. M. Reddy, J. Wilde, J.M. Peterson, D.D. Lofgreen, and S.M. Johnson, *J. Electron. Mater.* 41, 2957 (2012).
12. M. Reddy, D.D. Lofgreen, K.A. Jones, J.M. Peterson, W.A. Radford, J.D. Benson, and S.M. Johnson, *J. Electron. Mater.* 42, 3114 (2013).
13. M. Reddy, W.A. Radford, D.D. Lofgreen, K.R. Olsson, J.M. Peterson, and S.M. Johnson, *J. Electron. Mater.* (2014). (submitted).
14. A. Noda, H. Kurita, and R. Hirano, *Mercury Cadmium Telluride Growth, Properties and Applications*, ed. P. Capper and J. Garland (West Sussex: Wiley, 2011), pp. 21–49.
15. JX Nippon Mining & Metal Corporation, www.nikkometals. com, April 2014.
16. T. Aoki, Y. Chang, G. Badano, J. Zhao, C. Grein, S. Sivananthan, and D.J. Smith, *J. Crystal Growth* 265, 224 (2004).
17. Y. Chang, C.R. Becker, C.H. Grein, J. Zhao, C. Fulk, T. Cassellman, R. Kiran, X.J. Wang, E. Robinson, S.Y. An, S. Mallick, S. Sivananthan, T. Aoki, C.Z. Wang, D.J. Smith, S. Velicu, J. Zhao, J. Crocco, Y. Chen, G. Brill, P.S. Wijewarnasuriya, N. Dhar, R. Sporken, and V. Nathan, *J. Electron. Mater.* 37, 1171 (2008).
18. D. Chandra, F. Aqariden, J. Frazier, S. Gutzler, T. Orent, and H.D. Shih, *J. Electron. Mater.* 29, 887 (2000).
19. J.D. Benson, A.B. Cornfeld, M. Martinka, K.M. Singley, Z. Derzko, P.J. Shorten, J.H. Dinan, P.R. Boyd, F.C. Wolfgram, B.H. Johs, P. He, and J.A. Wollam, *J. Electron. Mater.* 25, 1406 (1996).
20. M. Zandian, J.M. Arias, J. Bajaj, J.G. Pasko, L.O. Bubulac, and R.E. DeWames, *J. Electron. Mater.* 24, 1207 (1995).
21. J.N. Johnson, L.A. Almeida, M. Martinka, J.D. Benson, and J.H. Dinan, *J. Electron. Mater.* 28, 817 (1999).
22. P. Moravec, V.G. Ivanits'ka, J. Franc, Z.F. Tomashik, V.M. Tomashik, K. Masek, P.I. Feychuk, L.P. Shcherbak, P. Hoschl, R. Grill, and J. Walter, *J. Electron. Mater.* 38, 1645 (2009).
23. C.K. Egan, P. Dabrowski, Z. Klusek, and A.W. Brinkman, *J. Electron. Mater.* 38, 1528 (2009).
24. H. Yoon, J.M. Van Scyoc, M.S. Goorsky, H. Hermon, M. Schieber, J.C. Lund, and R.B. James, *J. Electron. Mater.* 26, 529 (1997).